ARTICLE

Analysis of Snow Distribution and Displacement in the Bogie Region of a High-Speed Train

Zhihui Du[1], Mengge Yu[1,*], Jiali Liu[2] and Xiulong Yao[1]

[1]College of Mechanical and Electrical Engineering, Qingdao University, Qingdao, 266071, China

[2]National Engineering Research Center for High-Speed EMU, CRRC Qingdao Sifang Co., Ltd., Qingdao, 266111, China

*Corresponding Author: Mengge Yu. Email: yumengge0627@163.com

ABSTRACT

Snow interacting with a high-speed train can cause the formation of ice in the train bogie region and affect its safety. In this study, a wind-snow multiphase numerical approach is introduced for high-speed train bogies on the basis of the Euler-Lagrange discrete phase model. A particle-wall impact criterion is implemented to account for the presence of snow particles on the surface. Subsequently, numerical simulations are conducted, considering various snow particle diameter distributions and densities. The research results indicate that when the particle diameter is relatively small, the distribution of snow particles in the bogie cavity is relatively uniform. However, as the particle diameter increases, the snow particles in the bogie cavity are mainly located in the rear wheel pairs of the bogie. When the more realistic Rosin-Rammler diameter distribution is applied to snow particles, the positions of snow particles with different diameters vary in the bogie cavity. More precisely, smaller diameter particles are primarily located in the front and upper parts of the bogie cavity, while larger diameter snow particles accumulate at the rear and in the lower parts of the bogie cavity.

Nomenclature

$\overline{u}_j$	Average of the jth component of air velocity
x_j	The jth component of the rectangular coordinate
ρ	Air density
$\overline{u}_i$	Time average of the ith component of air velocity
$\overline{p}$	Time average of air pressure
x_i	The ith component of the rectangular coordinate
$\overline{\tau}_{ij}$	Time average of viscous stress tensor
$-\rho\overline{u'_i u'_j}$	Reynolds stress
u'_i	Pulsation value of ith component of air velocity
u'_j	Pulsation value of jth component of air velocity
M_i	The exchange the ith component for interphase momentum
μ_t	Turbulent viscosity

k	Turbulence kinetic energy
$\overline{u}_k$	Average of the kth component of air velocity
x_k	The kth component of the rectangular coordinate
δ_{ij}	Kronecker delta
ω	Specific dissipation
Γ_k	Effective diffusivity of k
G_k	Turbulence generator term of k
Y_k	Turbulent dissipation term of k
Γ_ω	Effective diffusivity of ω
G_ω	Turbulence generator term of ω
Y_ω	Turbulent dissipation term of ω
D_ω	Cross-diffusion terms
m_p	Particle mass
$\overrightarrow{u}_p$	Particle velocity
$\overrightarrow{u}$	Fluid velocity
ρ_p	Particle density
$\overrightarrow{F}$	Additional force
τ_r	Particle relaxation time $\tau_r = \dfrac{\rho_p d_p{}^2}{18\mu}\dfrac{24}{C_d \mathrm{Re}}$
d_p	Particle diameter
μ	Fluid viscosity
Re	The relative Reynolds number $\mathrm{Re} \equiv \dfrac{\rho d_p \left|\overrightarrow{u_p} - \overrightarrow{u}\right|}{\mu}$
U_{ref}	Train operating speed
Δt	Time step
Δx	Mesh size
d	Snow diameter
Y_d	The mass fraction of a snow particle with a diameter greater than d
$\overline{d}$	Average particle diameter
n	Particle diameter distribution parameter

1 Introduction

Due to its large capacity, high running speed, and low freight, railway transportation has become a crucial mode for both goods and people [1]. However, a snowy environment may result in various operational problems [2]. Snow accumulation on bogies can occur due to the wind-snow flow generated by railway vehicles operating on snow-covered routes in cold climates. This accumulation will impede the motion of the suspension system, potentially affecting the function of the braking mechanism.

The motion of snow has been analyzed in previous research by studying the characteristics of airflow. Guo et al. [3] systematically discussed the influence of the geometric complexity of bogies on train aerodynamics. You et al. [4] investigated the flow field in the bogie region under rotating wheel conditions. Xia et al. [5] studied the flow characteristics at the rear section of a train by using a separated vortex model. Zhang et al. [6] analyzed the impact of ground and wheel boundary conditions on train aerodynamics. It is certain that the airflow under the train will affect the motion of snow particles [7,8].

Computational fluid dynamics (CFD) has been a popular tool for predicting snowdrifts around buildings as computer technology has advanced [9–11]. The Euler-Euler and Euler-Lagrange models widely employed approaches, stand out among numerous multiphase flow models. The discrete phase model (DPM) has been proven to exhibit high precision in solving problems related to gas-solid two-phase flow [12,13].

Paradot et al. [14] employed DPM to compute snow accumulation on bogie and verified the results using experimental data. Wang et al. [15] analyzed the effect of bogie cavity shapes on snow accumulation and found that an inclined rear plate could reduce and prevent snow accumulation compared to a straight rear plate. Cai et al. [16] analyzed the impact of deflector devices on the motion of snow. Kamata et al. [17,18] investigated a method for estimating the amount of snow accretion on bogies. Wang et al. [19] studied the accumulation of snow and ice on non-powered bogies of urban rail trains and pointed out that the lower part of the bogie had more accretion amount than the upper part. Gao et al. [20,21] utilized the DPM to investigate the motion, accumulation, and flow of snow around bogie. Lan et al. [22] investigated the effect of various shapes of snow particles on snow accumulation in the bogie region and pointed out that using spherical snow particles would result in the most accumulation on the surfaces of the braking and suspension system. Clifton et al. [23], based on wind tunnel experiments, improved the snow saltation model using the Euler-Lagrange method. Zhang et al. [24] studied the impact of snow parameters on bogie snow accumulation using the Euler-Lagrange method.

Currently, most studies of snow accumulation on bogies employed uniform particle diameters. However, in nature, the diameters of snow particles are non-uniform [25]. Therefore, it is necessary to comprehensively explore the impact of diameter distribution on snow accumulation in the bogie region. This study establishes an aerodynamic model of the train bogie under snowy conditions, utilizing the Euler-Lagrange model. Additionally, it explores the effect of different particle diameter distributions and snow densities on the snow motion in the bogie region.

2 Numerical Methods

2.1 Continuous Phase Model

The train speed used in this study is 200 km/h (Ma < 0.3). Hence, the flow field surrounding the train adopts the steady incompressible Reynolds-averaged Navier-Stokes equation.

The continuous phase governing equations [26] include the mass Eq. (1) and the momentum Eq. (2):

$$\frac{\partial \overline{u}_j}{\partial x_j} = 0 \tag{1}$$

$$\rho \frac{\partial (\rho \overline{u}_j \overline{u}_i)}{\partial x_j} = -\frac{\partial \overline{p}}{\partial x_i} + \frac{\partial \overline{\tau}_{ij}}{\partial x_j} + \frac{\partial}{\partial x_j}(-\rho \overline{u'_i u'_j}) - M_i \tag{2}$$

where $\overline{u}_j$ is time average of the jth component of air velocity, x_j is the jth component of the rectangular coordinate, ρ is the air density, $\overline{u}_i$ is time average of the ith component of air velocity, $\overline{p}$ is the time average of air pressure, x_i is the ith component of the rectangular coordinate, $\overline{\tau}_{ij}$ is the time average of viscous stress tensor, $-\rho \overline{u'_i u'_j}$ is the Reynolds stress, u'_i is pulsation value of ith component of air velocity, u'_j is pulsation value of jth component of air velocity, M_i is the exchange the of the ith component for interphase momentum.

The Boussinesq hypothesis is a frequently used approach for connecting Reynolds stresses with mean velocity gradients:

$$-\rho \overline{u'_i u'_j} = \mu_t \left(\frac{\partial \overline{u}_i}{\partial x_j} + \frac{\partial \overline{u}_j}{\partial x_i} \right) - \frac{2}{3} \left(\rho k + \mu_t \frac{\partial \overline{u}_k}{\partial x_k} \right) \delta_{ij} \tag{3}$$

where μ_t is the turbulent viscosity, which depends on turbulence kinetic energy k and its rate of dissipation ε, $\overline{u}_k$ is time average of the kth component of air velocity, x_k is the kth component of the rectangular coordinate, δ_{ij} is Kronecker delta.

The *SST k-ω* model combines the computational advantages of both the *k-ω* and *k-ε* models, resulting in higher accuracy and reliability [27]. Its expression is:

$$\rho \frac{\partial(k\bar{u}_i)}{\partial x_i} = \frac{\partial}{\partial x_j}\left(\Gamma_k \frac{\partial k}{\partial x_j}\right) + G_k - Y_k \tag{4}$$

$$\rho \frac{\partial(\omega\bar{u}_i)}{\partial x_i} = \frac{\partial}{\partial x_j}\left(\Gamma_\omega \frac{\partial \omega}{\partial x_j}\right) + G_\omega - Y_\omega + D_\omega \tag{5}$$

where ω is the specific dissipation, Γ_k and Γ_ω are effective diffusivity of k and ω, respectively, G_k is the generation of k due to mean velocity, G_ω is generation of ω, Y_k and Y_ω are dissipation of k and ω due to turbulence, D_ω is cross-diffusion term.

The expressions for all additional constants (Γ_k, Γ_ω, G_k, G_ω, Y_k, Y_ω, and D_ω) are provided in reference [28] and will not be reiterated here.

2.2 Discrete Phase Model

The discrete phase is simulated using the Lagrange method. The current research assumes that snow particles are spheres, and the interaction between each snow particle is neglected. In addition, the snowy condition is simulated using a two-way coupled model [29,30]. The force balance equation is [31]:

$$m_p \frac{d\vec{u}_p}{dt} = m_p \frac{\vec{u} - \vec{u}_p}{\tau_r} + m_p \frac{\vec{g}(\rho_p - \rho)}{\rho_p} + \vec{F} \tag{6}$$

where m_p is particle mass, $\vec{u}_p$ is particle velocity, $\vec{u}$ is fluid velocity, ρ_p is particle density, ρ is fluid density, τ_r is particle relaxation time, and its expression is $\tau_r = \frac{\rho_p d_p^2}{18\mu} \frac{24}{C_d \text{Re}}$, d_p is particle diameter, μ is fluid viscosity, and Re is relative Reynolds number and its expression is $\text{Re} \equiv \frac{\rho d_p |\vec{u}_p - \vec{u}|}{\mu}$, $\vec{F}$ is the additional force, which includes the virtual mass and pressure gradient forces. In this study, the additional forces can be ignored.

The time step for a transient solution must fulfill a Courant number (CFL) smaller than 1 [32]. Based on Eq. (7), the time step for the transient is 5e-4s.

$$CFL = \frac{U_{ref}\Delta t}{\Delta x} \tag{7}$$

where U_{ref} is operating speed, Δt and Δx are the time step and mesh size, respectively.

2.3 Rosin-Rammler Diameter Distribution

The snow particle diameters are described using the Rosin-Rammler diameter distribution, which is expressed as follows:

$$Y_d = e^{-(d/\bar{d})^n} \tag{8}$$

where d is diameter of snow particles, Y_d is mass fraction of snow particles with a diameter greater than d, $\bar{d}$ is average particle diameter, and n is particle diameter distribution parameter.

3 Computational Model and Verification

3.1 Computational Domain and Meshing

The multiphase flow in a snowy condition is relatively complicated and requires a significant amount of calculation. A geometric model is established, consisting of a power bogie and a simplified train body. Fig. 1 illustrates the computational domain.
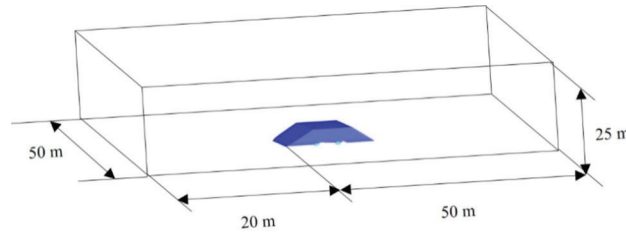

Figure 1: Computational domain

To achieve higher simulation accuracy, mixed meshes of hexahedral and tetrahedral are used to generate the mesh, and two refinement boxes are established around the train. The bogie and the train body surface are divided into ten boundary layers, with an initial height of 0.01 mm and a height ratio of 1.2. The computational mesh consists of approximately 26 million meshes. Fig. 2 displays the computational mesh.

3.2 Boundary Conditions and Simulation Settings

In this paper, a pressure-based solver was employed, and the pressure and velocity fields were coupled through the SIMPLE algorithm. For spatial discretization, diverse formats were utilized to handle different terms, ensuring the accuracy of the simulation. In the process of spatial discretization, the gradient item utilized a least-squares cell-based scheme, the pressure item employed a second-order scheme, and the momentum item, turbulent kinetic energy, and turbulent discretization rate were treated with a second-order upwind scheme. Additionally, to ensure temporal accuracy, a first-order implicit format was chosen for temporal discretization, ensuring stability and reliability in the numerical simulation along the time dimension. The continuous phase solution has 20 iterations per time step, with a time step of 5e-4s. The trajectory of the particle was simulated utilizing the unsteady particle tracking method, and an automatic tracking scheme was used.

Snow particles were released beneath the train body from an injection surface. As seen in Fig. 3, the injector was positioned under the bogie cavity, with a width of 4 m and a height of 0.4 m [33].

In the numerical simulation, a rotating wall was applied to the wheel with a rotating velocity of 120 rad/s. Table 1 presents the specific boundary conditions.

Two types of diameter distributions are used for snow particles: the uniform diameter distribution and the Rosin-Rammler diameter distribution. When employing the uniform diameter distribution, snow particle diameters are chosen to be 0.1, 0.2, 0.4, and 0.75 mm, respectively. When the Rosin-Rammler diameter distribution is adopted, this paper sets an average diameter of 0.4 mm for snow particles, with minimum and maximum diameters of 0.1 and 0.75 mm, respectively. The density of snow particles depends on latitude and snowfall duration, ranging from 50 to 500 kg/m^3 [34]. Consequently, the densities of snow particles are 50, 150, 250, 350, and 500 kg/m^3, respectively. The calculation conditions are displayed in Table 2.
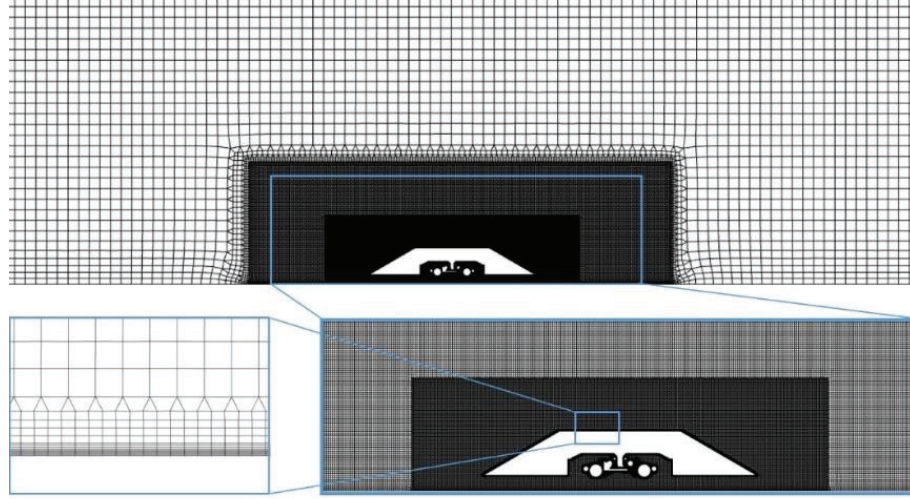
(a) Volume meshes
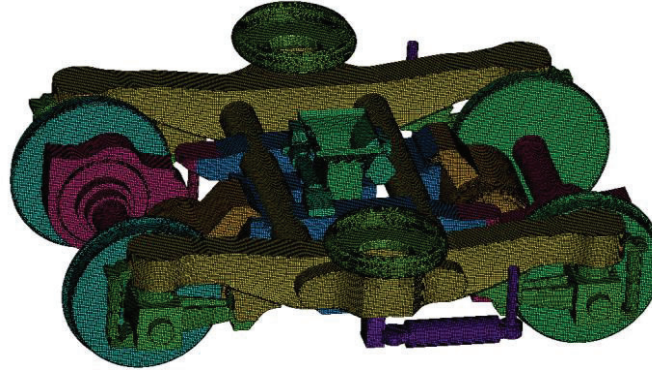
(b) Surface meshes

Figure 2: Computational mesh
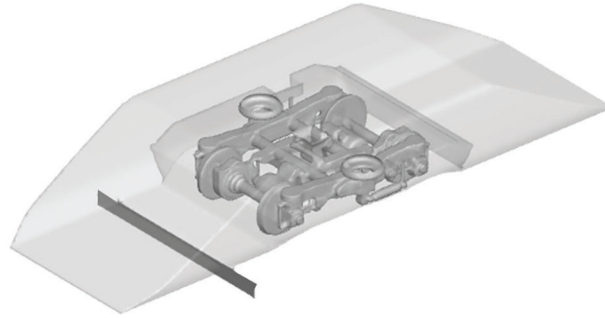
Figure 3: Arrangement of the particle injection

Snow particles may adhere, shear or bounce when they collide with the bogie surface. The criteria for capturing snow particles are proposed by Trenker et al. [35]. These criteria are associated with both the critical friction wind speed and the critical capture angle [36,37]. When the incident angle of particles exceeds the critical capture angle, a rebound phenomenon occurs, causing the particles to quickly leave the surface. Conversely, if the incident angle is smaller than the critical capture angle, the adhesion of

particles to the surface is determined based on the friction wind speed at the point of collision. This determination relies on comparing the friction wind speed of snow particles at the collision point with the designated critical friction wind speed. If the wind speed of friction is below the critical value, adhesion occurs; otherwise, the particles are blown away. To present the research results more clearly, Fig. 4 illustrates the impact results of snow particles on a surface. The critical capture angle is 60°, and the critical wind speed of friction is 1 m/s. Additionally, the normal rebound coefficient and tangential rebound coefficient are 0.01 and 0.2, respectively.

Table 1: Boundary condition setting

Boundary region	Boundary conditions of air phase	Boundary conditions of snow particle phase
Inlet	Velocity inlet	Escape
Outlet	Pressure outlet	Escape
Side-wall & up-wall	Symmetry	—
Ground	Moving wall: transition	Escape
Wheels	Moving wall: rotation	Reflect
Bogie (except wheels)	No-slip wall	UDF
Simplified train body	No-slip wall	Reflect

Table 2: Calculation condition of snow particle parameter change

Test	Diameter	Density	Test	Distribution	Density
1	0.1 mm	250 kg/m^3	5	Rosin-Rammler	250 kg/m^3
2	0.2 mm	250 kg/m^3	6	Rosin-Rammler	50 kg/m^3
3	0.4 mm	250 kg/m^3	7	Rosin-Rammler	150 kg/m^3
4	0.75 mm	250 kg/m^3	8	Rosin-Rammler	350 kg/m^3
5	Rosin-Rammler	250 kg/m^3	9	Rosin-Rammler	500 kg/m^3

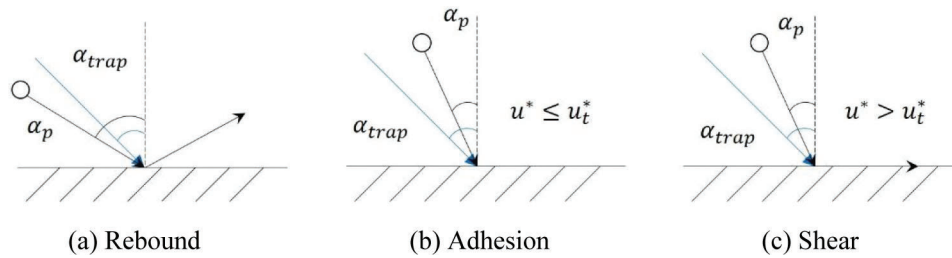(a) Rebound   (b) Adhesion   (c) Shear

Figure 4: Impact results of snow particles on a surface

3.3 Mesh Independence Verification

To validate the independence of the mesh, this study employs three meshes with different parameters (coarse, medium and fine mesh). The boundary layer settings remain consistent across all three meshes, with the only difference being in the mesh parameters for the train surface and refinement boxes. Table 3

presents the key parameters for each mesh set. The pressure coefficients along the centerline, positioned 0.2 m below the bottom of the train, are calculated for the three meshes [38], as shown in Fig. 5. When compared to the results obtained using the fine mesh, the maximum error observed with the coarse mesh is 6.3%, while that with the medium mesh is 2.6%. To balance computational efficiency and accuracy, the medium mesh is selected for subsequent simulation calculations.

Table 3: Mesh information

Computational mesh	Simplified train surface mesh (mm)	Bogie surface mesh (mm)	Mesh total (million)
Coarse mesh	22	11	20
Medium mesh	20	10	26
Fine mesh	18	9	33
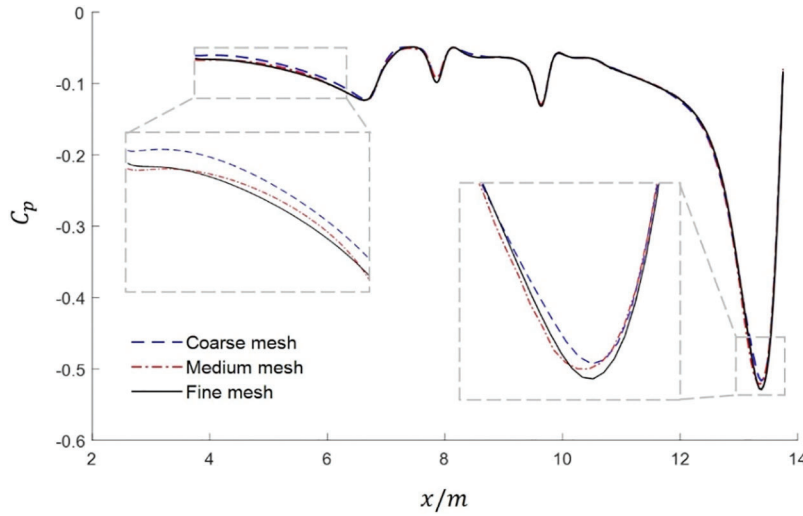
Figure 5: Pressure coefficients along the centerline under the bogie

4 Results and Discussion

This study employs a method to extract three key slices for analyzing flow characteristics. These slices are positioned at the central locations of the wheel, gearbox, and bogie, ensuring comprehensive coverage of flow characteristics in critical areas. Fig. 6 clearly illustrates the exact locations of these three slices.

4.1 Flow Field Characteristic Analysis

Fig. 7 shows the velocities and streamlines in the bogie region at three designated slice positions. When the airflow bypasses the bottom of the bogie, an upward airflow is created behind the rear wheel at Slice 1, following the wheel's rotation. Furthermore, due to the lower position of the wheel compared to the train body, when airflow impacts the windward side of the lower wheel, it is more likely to flow upward, leading to only one vortex formed above the front section of the rear wheel. As can be seen from Slice 2, a vortex is generated at the front wheel axle as the wheel rotates. Due to the small distance between the gearbox and the rear end plate, a vortex is generated in that space. On Slice 3, two vortices are generated, one located above the front motor and the other in front of the rear motor. Due to the large gap between the rear motor and the rear end plate, the airflow is more likely to flow out of the bogie cavity.
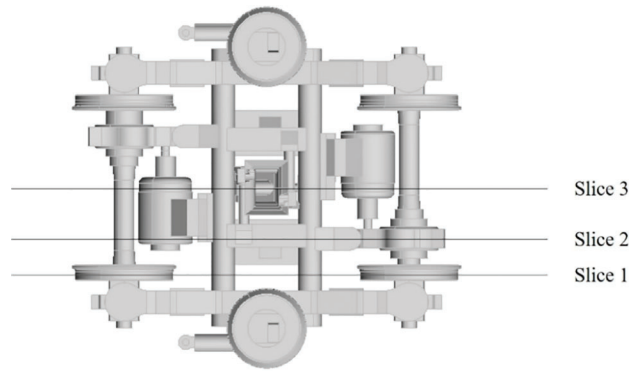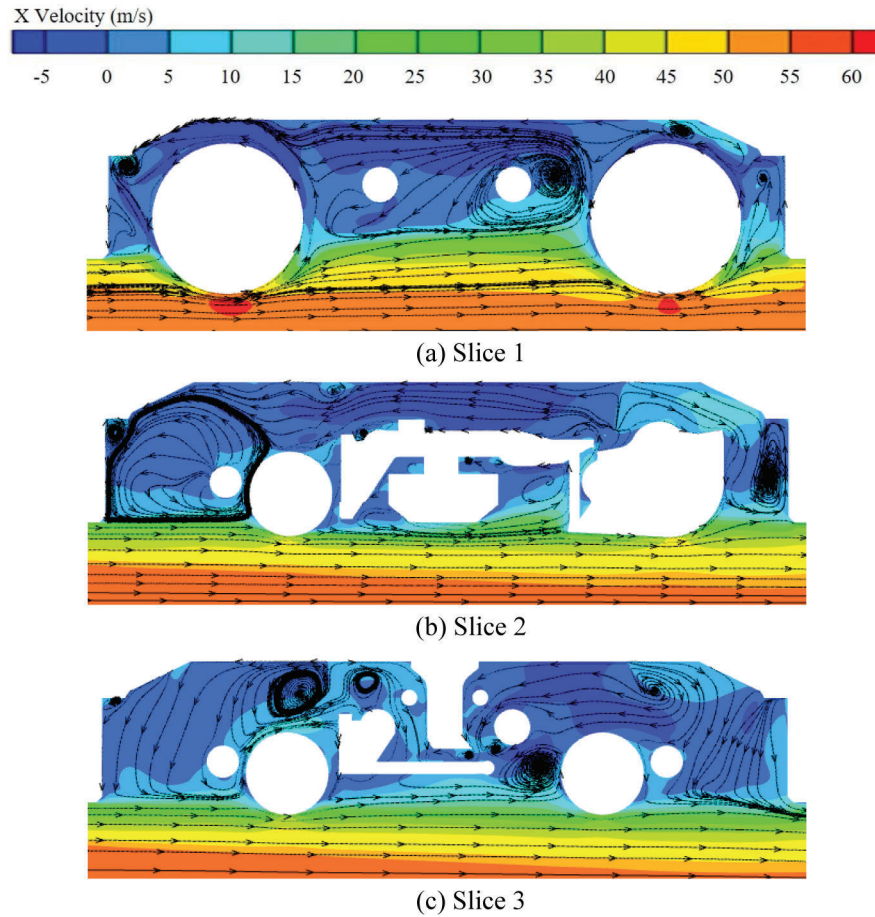
Figure 6: Positions of slices in bogie region

(a) Slice 1

(b) Slice 2

(c) Slice 3

Figure 7: Flow velocity and streamline distribution in the bogie region

4.2 Effect of Different Particle Diameter Distributions on Snow Motion

Fig. 8 illustrates the distribution of snow with different diameters. When snow particle diameter is 0.1 or 0.2 mm, influenced by the rear wheels, the snow will cover the entire bogie cavity. As the bogie is positioned lower than the train body, an upward trend in the motion of snow particles is observed when they reach the front motor area of the bogie. As the particles diameter increases, their ability to move upward around the front motor of the bogie decreases due to gravity. However, some snow particles may still enter the bogie

cavity due to the rear wheels. Thus, when the diameter of the snow particles is large, they are mainly located in the rear wheel pairs of the bogie.
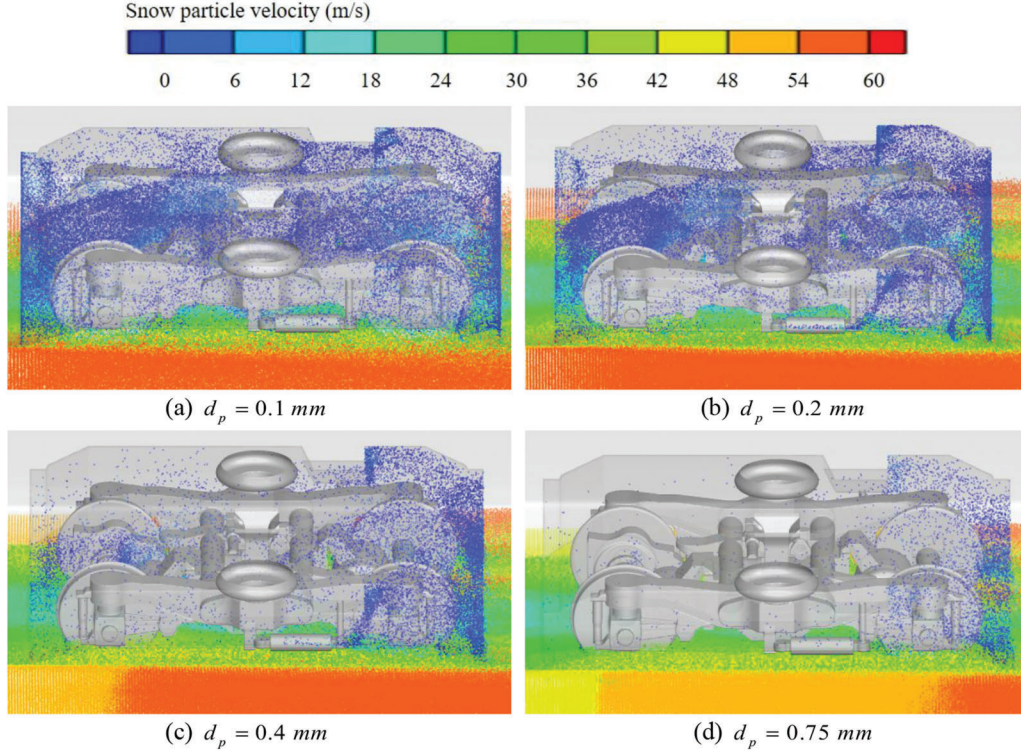

Figure 8: Distribution of snow with different diameters

Snow distribution resembles that of small snow particles when using the Rosin-Rammler diameter distribution to simulate the snow particles. However, a higher concentration of snow particles is observed on the rear end plate, as shown in Fig. 9. When adopting the Rosin-Rammler diameter distribution, small diameter particles are mainly located at the front of the bogie cavity, whereas in the rear part, both small and large diameter particles coexist. Therefore, the concentration of snow is greater at the rear than at the front.

Fig. 10 shows the concentration of snow particles with various particle diameters at different slices. As the particle diameter increases, gravity plays an increasingly significant role in particle movement. As a result, a lower concentration of snow is observed in the upper part. When the particle diameter is 0.75 mm, only a few particles are present at the rear. When utilizing the Rosin-Rammler diameter distribution, the concentration distribution of snow is comparable to that of snow particles with a 0.2 mm diameter. However, the concentration of snow on the rear end plate is greater than that of particles with a 0.2 mm diameter.

4.3 Effect of Snow Density on Snow Motion

The latitude and duration of snow accumulation have an impact on the density of snow. For the purposes of this study, various snow particle densities are selected for simulation. The calculation results are shown in Fig. 11, with Fig. 9 illustrating a snow density of 250 kg/m^3. Under lower-density conditions, snow particles are able to rise after impacting the bogie. When the density of 50 kg/m^3, more snow particles are observed at the front of the bogie cavity. It should be noted that low density, especially 50 kg/m^3, is present only briefly in newly formed dry snow particles. As the particle density increases, a higher snow concentration is observed in the rear part.
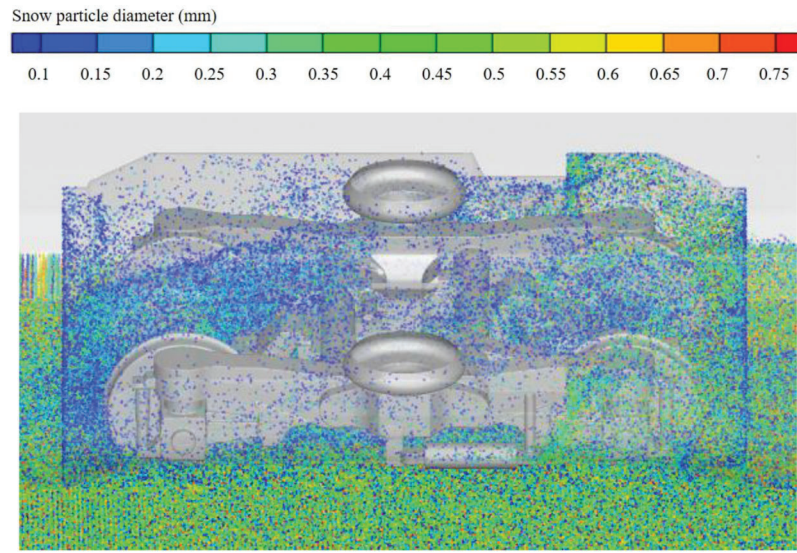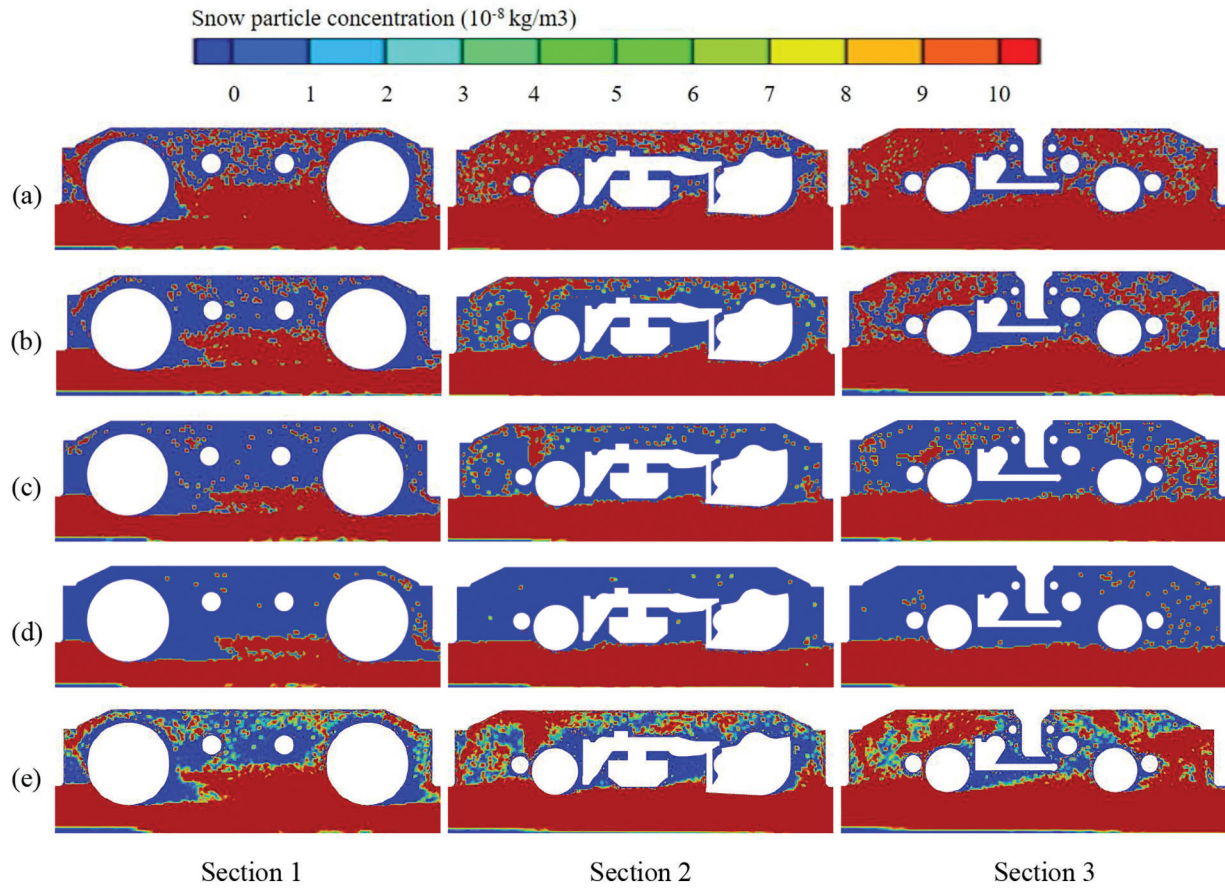
Figure 9: Distribution of snow particle diameters

Figure 10: Distribution of snow concentration with different diameters at the slices: (a) $d_p = 0.1\,mm$, (b) $d_p = 0.2\,mm$, (c) $d_p = 0.4\,mm$, (d) $d_p = 0.75\,mm$, (e) the Rosin-Rammler diameter distribution
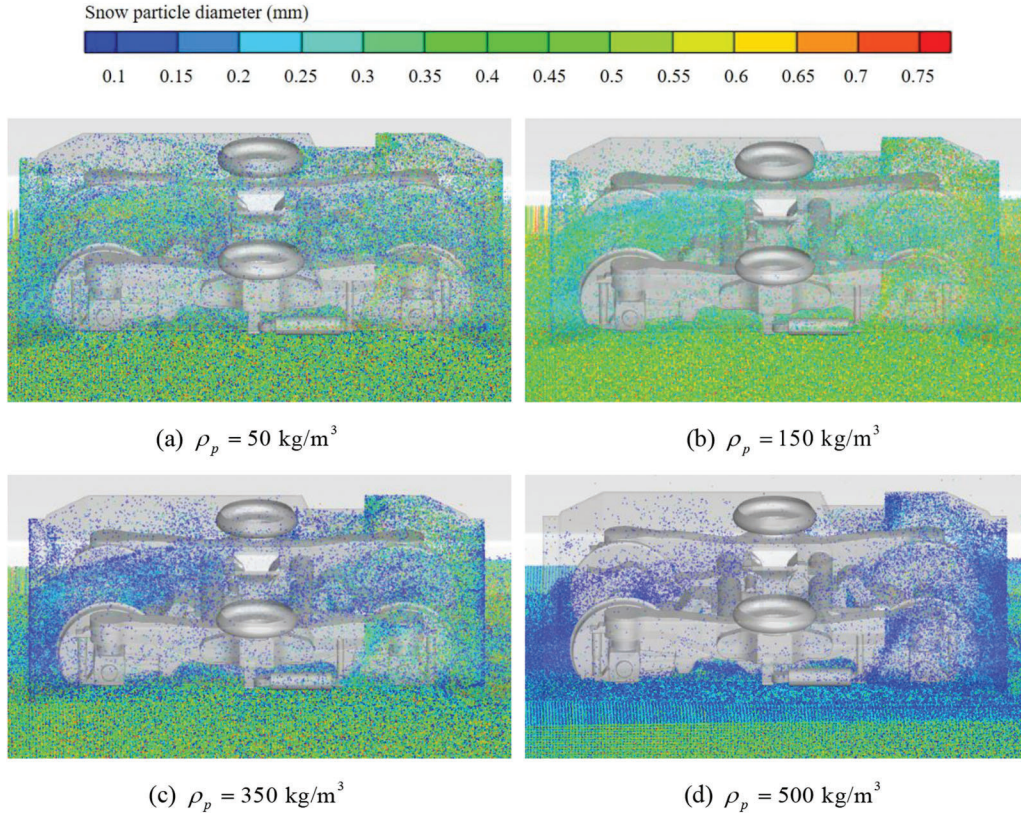
Figure 11: Distribution of snow particle diameters with different densities

When the snow density of 50 kg/m^3, there is a higher probability of larger diameter particles entering the bogie cavity because of the lower gravity. However, with a density of 150 kg/m^3, larger diameter particles in the bogie cavity are predominantly found in the rear wheel pairs of the bogie due to increased gravity. When the density is 350 kg/m^3, the impact of gravity becomes more significant. It has been observed that smaller diameter particles are mainly located in the front and upper parts of the bogie cavity, while larger diameter snow accumulation is in the rear and lower parts of the bogie cavity. When the density reaches 500 kg/m^3, the increased gravity prevents snow particles with a larger diameter from entering the bogie cavity. At the bottom, snow stratifies due to gravity, with larger particles mainly accumulating in the lower layer.

Fig. 12 displays the concentrations of snow at various densities in the bogie region at different slices. As particle density increases, a lower snow concentration is observed in the upper part of the bogie cavity. At a density of 50 kg/m^3, the concentration is relatively high in all slices. However, at a density of 500 kg/m^3, fewer snow particles are present in the bogie cavity, and most of them accumulate at the bottom. When the densities of snow particles are 150, 250, and 350 kg/m^3, the concentration distributions are similar. In Slice 1, the concentration of snow particles is relatively high between the two wheels. In Slice 2, the snow particles mainly accumulate in the low-speed vortices located at the front wheel axle and the rear of the gearbox. In Slice 3, the snow particles mainly accumulate in the vortices above the front motor, in front of the rear motor, and on the rear end plate of the bogie cavity.
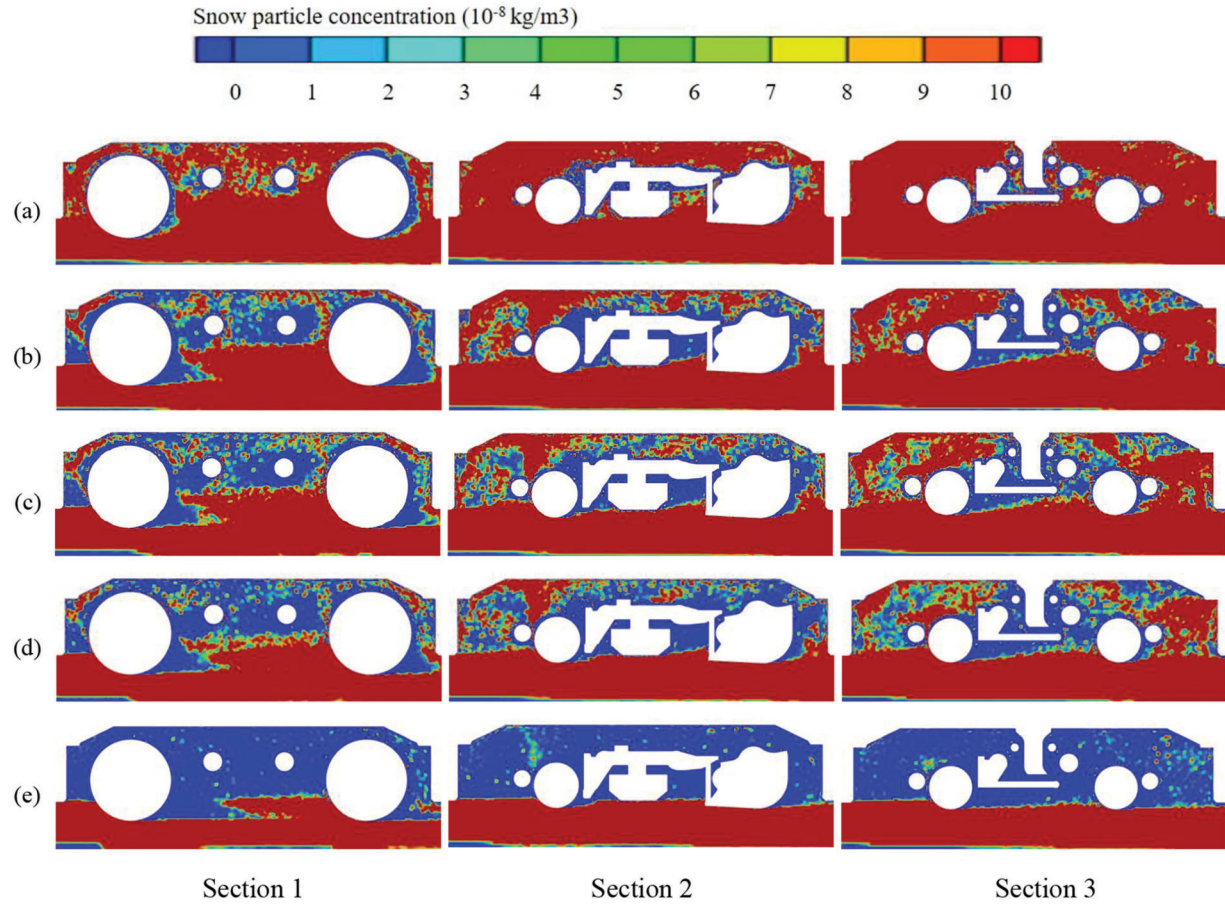
Figure 12: Distribution of snow particle concentration with different diameters at the slices: (a) $\rho_p = 50\,\mathrm{kg/m^3}$, (b) $\rho_p = 150\,\mathrm{kg/m^3}$, (c) $\rho_p = 250\,\mathrm{kg/m^3}$, (d) $\rho_p = 350\,\mathrm{kg/m^3}$, (e) $\rho_p = 500\,\mathrm{kg/m^3}$

5 Conclusion

1. When the uniform diameter distribution is applied to simulate snow particles, small diameter particles cover the entire bogie cavity. As the particle diameter increases, the impact of gravity becomes more significant. Therefore, larger snow particles are mainly situated around the rear wheels.

2. When the Rosin-Rammler diameter distribution is used to simulate snow particles, the positions of particles with various diameters vary in the bogie cavity. Smaller diameter particles are mainly located in the front and upper parts of the bogie cavity, while larger diameter particles accumulate in the rear and lower parts of the bogie cavity.

3. Within a certain range, the variation in snow particle density has a small influence on snow distribution. The decrease in the diameter of particles in the bogie cavity is observed as the particle density increases.

4. As the diameter and density increase, a lower snow concentration is observed in the upper part.

Author Contributions: The authors confirm their contribution to the paper as follows: study conception and design: D. Z and Y. M; data collection: D. Z and Y. X; analysis and interpretation of results: D. Z, Y. M and L. J; draft manuscript preparation: D. Z. All authors reviewed the results and approved the final version of the manuscript.

Availability of Data and Materials: All the data used in the study are included in the manuscript.

Conflicts of Interest: The authors declare that they have no conflicts of interest to report regarding the present study.

References

1. Li T, Liang H, Zhang J, Zhang J. Numerical study on aerodynamic resistance reduction of high-speed train using vortex generator. Eng Appl Comp Fluid. 2023;17(1):e2153925.
2. Kloow L, Jenstav M. High-speed train operation in winter climate. Transrail Publication BVF5. 2011;2:1–77.
3. Guo Z, Liu T, Chen Z, Xia Y, Li W, Li L. Aerodynamic influences of bogie's geometric complexity on high-speed trains under crosswind. J Wind Eng Ind Aerod. 2020;196:104053.
4. You J, Chen Y, Yang Z. Influence of the wheel rotation on underbody flow and aerodynamic forces of high speed train. Procedia Eng. 2015;126:399–404.
5. Xia C, Wang H, Shan X, Yang Z, Li Q. Effects of ground configurations on the slipstream and near wake of a high-speed train. J Wind Eng Ind Aerod. 2017;168:177–89.
6. Zhang J, Li JJ, Tian HQ, Gao GJ, Sheridan J. Impact of ground and wheel boundary conditions on numerical simulation of the high-speed train aerodynamic performance. J Fluid Struct. 2016;61:249–61.
7. Paz C, Suárez E, Gil C, Cabarcos A. Effect of realistic ballasted track in the underbody flow of a high-speed train via CFD simulations. J Wind Eng Ind Aerod. 2019;184:1–9.
8. García J, Crespo A, Berasarte A, Goikoetxea J. Study of the flow between the train underbody and the ballast track. J Wind Eng Ind Aerod. 2011;99(10):1089–98.
9. Tominaga Y. Computational fluid dynamics simulation of snowdrift around buildings: past achievements and future perspectives. Cold Reg Sci Technol. 2018;150:2–14.
10. Beyers M, Waechter B. Modeling transient snowdrift development around complex three-dimensional structures. J Wind Eng Ind Aerod. 2008;96(10–11):1603–15.
11. Uematsu T, Nakata T, Takeuchi K, Arisawa Y, Kaneda Y. Three-dimensional numerical simulation of snowdrift. Cold Reg Sci Technol. 1991;20(1):65–73.
12. Chiesa M, Mathiesen V, Melheim JA, Halvorsen B. Numerical simulation of particulate flow by the Eulerian-Lagrangian and the Eulerian-Eulerian approach with application to a fluidized bed. Comput Chem Eng. 2005;29(2):291–304.
13. Pankajakshan R, Mitchell BJ, Taylor LK. Simulation of unsteady two-phase flows using a parallel Eulerian-Lagrangian approach. Comput Fluids. 2011;41(1):20–6.
14. Paradot N, Allain E, Croué R, de La Casa X, Pauline J. Development of a numerical modelling of snow accumulation on a high speed train. In: International Conference on Railway Technology: Research, Development and Maintenance, 2014; Scotland: Stirlingshire.
15. Wang J, Zhang J, Zhang Y, Xie F, Krajnović S, Gao G. Impact of bogie cavity shapes and operational environment on snow accumulating on the bogies of high-speed trains. J Wind Eng Ind Aerod. 2018;176:211–24.
16. Cai L, Lou Z, Li T, Zhang J. Numerical study on the effects of anti-snow deflector on the wind-snow flow underneath a high-speed train. J Appl Fluid Mech. 2020;14(1):287–99.
17. Kamata Y. Climatic conditions causing snow accretion on Shinkansen bogies. Railw Technol Newsletter. 2014;48:286.
18. Kamata Y, Yokokura A. Estimation method of snow accretion amount on train bogies. In: IWAIS, 2019; Reykjavík, Iceland.

19. Wang T, Wang Y, Gao G, Zhao C, Jiang C. Experimental investigations on the performance of anti-snow designs for urban rail train bogies. J Wind Eng Ind Aerod. 2022;221:104913.

20. Gao G, Zhang Y, Xie F, Zhang J, He K, Wang J, et al. Numerical study on the anti-snow performance of deflectors in the bogie region of a high-speed train using the discrete phase model. P I Mech Eng F-J Rai. 2019;233(2):141–59.

21. Gao G, Zhang Y, Miao X, Wang J, Zhang J, Jiang C. Influence of bogie fairing configurations on the snow accretion around bogie regions of a high-speed train under crosswind conditions. Mech Based Des Struct. 2023;51(10):5452–69.

22. Lan H, Cai L, Zhang J, He P. Research on movement and deposition of snow particles with different shapes in the bogie region. P I Mech Eng F-J Rai. 2023;237(5):669–79.

23. Clifton A, Lehning M. Improvement and validation of a snow saltation model using wind tunnel measurements. Earth Surf Proc Land. 2008;33(14):2156–73.

24. Zhang L, Li T, Cai L, Zhang JY, An C. Effect of snow parameters on snow accumulation in high-speed train bogies. J Mech Eng. 2020;56(10):216–24 (In Chinese).

25. Langlois A, Royer A, Montpetit B, Roy A, Durocher M. Presenting snow grain size and shape distributions in northern Canada using a new photographic device allowing 2D and 3D representation of snow grains. Front Earth Sci. 2020;7:347.

26. Versteeg HK, Malalasekera W. An introduction to computational fluid dynamics: the finite volume method. Upper Saddle River, NJ: Pearson Education Limited; 2007.

27. Li T, Qin D, Zhang J. Effect of RANS turbulence model on aerodynamic behavior of trains in crosswind. Chin J Mech Eng. 2019;32:1–12.

28. Fluent A. ANSYS fluent theory guide. Pittsburgh, Pennsylvania: ANSYS Inc.; 2021.

29. Yu M, Liu J, Dai Z. Aerodynamic characteristics of a high-speed train exposed to heavy rain environment based on non-spherical raindrop. J Wind Eng Ind Aerod. 2021;211:104532.

30. Yu M, Sheng X, Liu J, Huo W, Li M. Effects of wind-rain coupling on the aerodynamic characteristics of a high-speed train. J Wind Eng Ind Aerod. 2022;231:105213.

31. Batchelor GK. An introduction to fluid dynamics. Sword Bridge Town, England: Cambridge University Press; 1967.

32. Wang S, Bell JR, Burton D, Herbst AH, Sheridan J, Thompson MC. The performance of different turbulence models (URANS, SAS and DES) for predicting high-speed train slipstream. J Wind Eng Ind Aerod. 2017;165:46–57.

33. Cai L, Lou Z, Li T, Zhang J. Numerical study of dry snow accretion characteristics on the bogie surfaces of a high-speed train based on the snow deposition model. Int J Rail Transp. 2022;10(3):393–411.

34. Zhang G, Zhang Q, Fan F, Shen S. Research on snow load characteristics on a complex long-span roof based on snow-wind tunnel tests. Appl Sci. 2019;9(20):4369.

35. Trenker M, Payer W. Investigation of snow particle transportation and accretion on vehicles. In: 24th AIAA Applied Aerodynamics Conference, 2006; San Francisco, USA. p. 3648.

36. Liston GE, Sturm M. A snow-transport model for complex terrain. J Glaciol. 1998;44(148):498–516.

37. Sato T, Kosugi K, Mochizuki S, Nemoto M. Wind speed dependences of fracture and accumulation of snowflakes on snow surface. Cold Reg Sci Technol. 2008;51(2–3):229–39.

38. Li T, Dai Z, Yu M, Zhang W. Numerical investigation on the aerodynamic resistances of double-unit trains with different gap lengths. Eng Appl Comp Fluid. 2021;15(1):549–60.